Journal of Micromechanics and Microengineering

PAPER

Integration of buried piezoresistive sensors and PZT thin film for dynamic and static position sensing of MEMS actuator

To cite this article: Andrea Vergara *et al* 2020 *J. Micromech. Microeng.* **30** 115020

IOP Publishing Journal of Micromechanics and Microengineering
J. Micromech. Microeng. **30** (2020) 115020 (8pp) https://doi.org/10.1088/1361-6439/abb756

Integration of buried piezoresistive sensors and PZT thin film for dynamic and static position sensing of MEMS actuator

Andrea Vergara[1], **Takashiro Tsukamoto**[1], **Weileun Fang**[2] and **Shuji Tanaka**[1]

[1] Department of Robotics, Tohoku University, Sendai, 980-8579, Japan
[2] Power Mechanical Engineering, National Tsing Hua University, Hsinchu 30013, Taiwan

E-mail: t_tsuka@mems.mech.tohoku.ac.jp

Received 4 June 2020, revised 19 August 2020
Accepted for publication 10 September 2020
Published 28 September 2020

CrossMark

Abstract

We developed a lead zirconate titanate (PZT) thin film actuator integrated with buried piezoresistors for the dynamic and static deformation sensing of a PZT MEMS actuator. We demonstrated the fabrication of sol-gel deposited PZT thin film devices combined with buried piezoresistors and proved, for the first time, the process compatibility of these materials. Dopant concentration measured by secondary ion mass spectrometry (SIMS) analysis confirms that the piezoresistor was successfully buried into the device. Motion detection of the fabricated MEMS cantilever actuated by the PZT thin film was successful and consistent with optical measurement as well as design values. From these results, we can conclude that our PZT actuator and piezoresistive sensors can be monolithically integrated. The fabrication process developed here can be used for high-stability piezoelectric MEMS actuators with feed-back control of position.

Keywords: buried piezoresistor, thin-film piezoelectric actuator, lead zirconate titanate (PZT), sensor-actuator integration

(Some figures may appear in colour only in the online journal)

1. Introduction

Lead zirconate titanate (PZT) is a popular material for piezoelectric MEMS and very competitive when voltage signal, force or power output is demanded [1]. The largest group in the piezoelectric device market are actuators/piezo-generators and is expected to expand rapidly in the near future [2].

The most successful piezoelectric actuators so far are the ink-jet printer heads, commercialized in the early 2000s and now considered as the standard technology. The advantages of piezoelectric actuation such as large force potential, high energy conversion efficiency, high energy density and fast dynamic response time have motivated continuous efforts to develop actuators for a wide range of applications. These include piezoelectric micro-motors [3], micro-pumps [4], radio frequency (RF) MEMS switches [5–8], acoustic transducers [9–13] and others. For thin film PZT MEMS loudspeakers, several patents have been granted to USound GmbH [14–16].

Several piezoelectric MEMS actuators for optical devices have been also developed, such as focus lens [17, 18] and scanning micromirrors [19–21]. Kanno [22] identified the deposition of high-quality film as one of the core technologies of piezoelectric MEMS. Indeed, companies such as Stanley Electric and FUJIFILM have developed PZT-based micromirrors achieving good performance by novel fabrication techniques [23] and additional impurities [24]. These devices have PZT-based sensors installed.

However, it is difficult to keep a static angle by this configuration, which is required for some applications. Also, as

Holström *et al* [25] indicated, achieving linear scanning and precision for high performance displays is quite challenging in piezoelectric devices. Moreover, the degradation of PZT thin film's properties by repeated actuation, often called 'electrical fatigue', has been reported by several groups such as Lou and Wang [26] and Mazzalai *et al* [27]. This phenomenon leads to poor long-term reliability and constitutes an obstacle when developing devices for commercial use.

Bell *et al* [28] observed that piezoresistive sensors have good resolution, dynamic range and response frequency compared to other MEMS sensors. Therefore, applying feedback control using silicon piezoresistive sensors is a potential solution. Sasaki *et al* [29] developed an integrated piezoresistive rotation angle sensor for feedback control of an electrostatic micromirror device. Yalcinkaya *et al* [30] developed an electromagnetic MEMS mirror with an integrated piezoresistive position sensor, which was successfully commercialized by MicroVision Inc. However, there is no detailed report about the integration of a PZT actuator and piezoresistive sensors.

In this paper, we propose a fabrication process to monolithically integrate the PZT actuator and the piezoresistive deformation sensor for the first time. Figure 1 shows the design concept of the device. The integration of the actuator and the sensor is a key for the proposed actuator system, in which the integrated sensor measures the displacement during actuation and the detected position signal is used for the feedback control to compensate the instability and non-linearity of the PZT thin film.

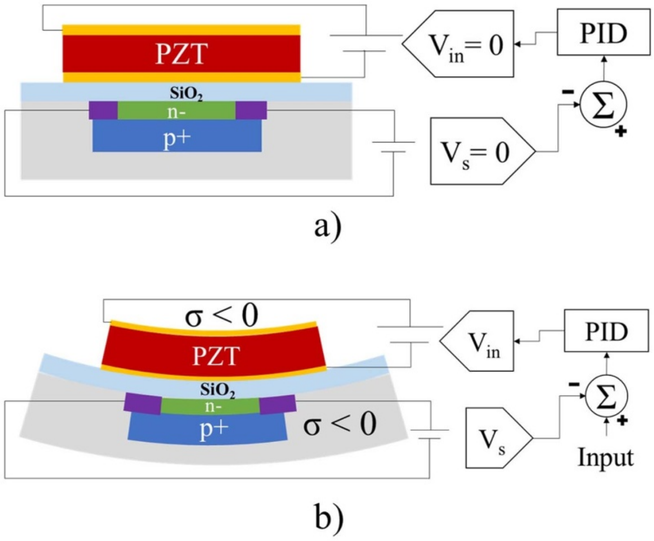

Figure 1. Design concept for PZT stable actuator. (a) Rest position, (b) actuation with feedback control system.

2. Design

To simplify the evaluation, a cantilever structure was chosen for the device. The piezoelectric actuator and piezoresistive sensors are monolithically integrated in the cantilever.

2.1. Working principle

Figure 2 shows the schematic of the PZT/piezoresistor device. A thin film of sol-gel PZT actuates the cantilever. For displacement sensing we chose the buried piezoresistive sensor developed by Esashi *et al* [31] because of its high stability and small footprint. This sensor's characteristic feature is that a thin layer of n-type Si covers the resistor, which lays deep into the substrate, minimizing the negative effects of impurities in the surface. The buried piezoresistor has been used for sensing [32], however this is the first report on it combined with piezoelectric actuators.

There are four buried piezoresistors in the device to form a Wheatstone bridge. Two piezoresistors are placed at the root of the cantilever, R_1 and R_2, while the other two, R_3 and R_4, are away from the cantilever. The PZT thin film was placed on the cantilever.

Resistivity changes ($\Delta R/R$) in piezoresistors can be modeled as

$$\frac{\Delta R}{R} = \frac{1}{2}(\pi_{11} + \pi_{12} + \pi_{44})\sigma, \tag{1}$$

where π_{11}, π_{12} and π_{44} are the piezoresistive constants and σ the applied stress.

When the voltage is applied to the PZT film, the cantilever deforms. Only R_1 and R_2 will be subjected to stress during actuation and its magnitude is assumed to be the same for both, so the output voltage from the Wheatstone bridge becomes

$$V_{\text{out}} = \left(\frac{0.5(\pi_{11} + \pi_{12} + \pi_{44})\sigma}{2 + 0.5(\pi_{11} + \pi_{12} + \pi_{44})\sigma} \right) G V_{\text{bias}}, \tag{2}$$

where G is the amplification gain and V_{bias} is the input voltage of the Wheatstone bridge.

Note that the output (V_{out}) is expected to be very small without electronic amplification, as it will always be a fraction of V_{bias}. Some cantilever parameters and material properties used for design are shown in table 1.

2.2. Sensitivity

To estimate the scale factor of the sensors, one way is to calculate it analytically. Since the structure is a simple beam with one end fixed and the other free, the maximum stress at the fixed end by bending can be written as

$$\sigma_{\text{max}} = -\frac{3Eh}{2\,L^2} z, \tag{3}$$

where E, L, h and z are the Young's modulus, the cantilever's length, the beam thickness and the displacement at free end, respectively. Substituting σ from equation (3) into equation (2) and taking $V_{\text{bias}} = 1$ V, $z = 1$ μm and gain $G = 1$, theoretical sensitivity becomes 0.158 mV μm^{-1}.

To account for the geometry and location of the piezoresistors, correction factors such as the ones used by Tsukamoto *et al* [32] for depth (C_{depth}) and length (C_{length}) was considered as

$$C_{\text{depth}} = \frac{\sigma_{\text{avg,d}}}{\sigma_{\text{max}}}$$

Table 1. Device's design parameters and material properties.

Parameter	Variable	Value	Unit
Cantilever length	L	1.5×10^{-3}	[m]
Cantilever width (base)	w_b	6×10^{-4}	[m]
Cantilever width (end)	w	4×10^{-4}	[m]
Cantilever thickness	h	1×10^{-5}	[m]
Young's modulus (Si)	E	1.7×10^{11}	[Pa]
Piezoresistor length	l_p	1.2×10^{-4}	[m]
Piezoresistor minimum depth	d_1	5×10^{-7}	[m]
Piezoresistor maximum depth	d_2	2×10^{-6}	[m]
Longitudinal piezoresistive coefficient [33–35]	$0.5(\pi_{11}+\pi_{12}+\pi_{44})$	3.5×10^{-10}	[Pa^{-1}]
PZT actuator thickness	–	1×10^{-6}	[m]

$$= \frac{\int_{d2}^{d_1}(1-\frac{2x}{h})\mathrm{d}x}{d_2-d_1} = 1-\frac{d_1+d_2}{h} \quad (4)$$

and

$$C_{\text{length}} = \frac{\sigma_{\text{avg,l}}}{\sigma_{\max}} = \frac{\int_{l_p}^{0}(1-\frac{2x}{L})\mathrm{d}x}{l_p} \quad (5)$$

$$= 1-\frac{l_p}{L}, \quad (6)$$

where d_1, d_2 and l_p are the buried piezoresistor minimum depth, maximum depth and length respectively. By multiplying the maximum theoretical output by C_{depth} and C_{length}, the estimated sensitivity becomes 0.109 mV μm^{-1}.

To obtain a more accurate value, finite element analysis (FEA) was used. COMSOL was used as the solver. Figure 3 shows the static analysis of the model, where the metal electrodes were not modeled. The voltage is applied to the PZT film so that the tip displacement of the cantilever becomes 1 μm. The stress tensor in y direction was measured at the position of piezoresistors. The average stress at the sensor is 0.208 MPa. By replacing this stress in equation (2), estimated sensitivity by FEA is 0.0365 mV μm^{-1}, about 33.4% of the previous estimation by analytic calculation.

The first resonant frequency, corresponding to the beam bending up and down, is found at 6.768 kHz according to modal analysis.

3. Fabrication

Figure 4 shows the proposed fabrication process. The device was fabricated on a SOI wafer, of which the thickness, crystal direction, doping type and resistivity of the device layer are 10 μm, $<1\,0\,0>$, N-type and $3\sim5\ \Omega\cdot$cm, respectively.

First, the buried piezoresistors were formed. Dry thermal oxidation was done to grow a thin oxide film of about 40 nm thickness (figure 4(a)) and then the buried piezoresistors were made by ion implantation in three steps. First implantation was light boron doping for the piezoresistors followed by annealing to drive in the dopants deeper into the substrate (figure 4(b)). Second implantation was heavy boron doping with split dose/energy for electrical contact and wiring (figure 4(c)). And last was phosphorus implantation (to make a shallow n-type layer to bury the sensors) followed by rapid thermal annealing to activate the dopants (figure 4(d)) [32]. Detailed conditions are shown in table 2.

Table 2. Buried piezoresistor fabrication details.

Process	Condition
First implantation (B)	3×10^{14}/cm^2 – 80 keV
Annealing	4 hours at 1100 °C in N_2
Second implantation (B)	2.5×10^{15}/cm^2 – 40 keV
	3×10^{15}/cm^2 – 100 keV
Third implantation (P)	1×10^{16}/cm^2 – 100 keV
Rapid thermal annealing	30 s at 1000 °C in N_2

Then the piezoelectric actuator was formed. A Pt thin film was deposited by sputtering at high temperature (600 °C) to form the bottom electrode for the PZT film. One micron of PZT thin film was deposited by the sol-gel method (figure 4(e)), similar to the process used by Moriyama *et al* [36], except that Ti was used as an adhesion layer instead of annealing the Pt film. PZT and Pt thin films were patterned by wet etching and ion beam milling (figure 4(f)), respectively. The SiO_2 film was patterned by wet etching using a buffered hydrofluoric acid (BHF) solution to make vias for the sensors (figure 4(g)). Then Au was deposited by vacuum evaporation and patterned by lift-off process to make the top electrode and contact pads.

Device layer Si was etched by DRIE from the topside to define the shape of cantilever (figure 4(h)). Finally, the handle layer and the buried oxide layer were etched by DRIE and CCP-RIE, respectively, to release the structure (figure 4(i)). The finished device is shown in figure 5. After packaging and wiring, the PZT film was poled for 5 minutes at 120 °C and 5 V.

4. Evaluation

The concentrations of dopants were confirmed by secondary ion mass spectrometry (SIMS) analysis. Figure 6 shows the measured concentrations of boron and phosphorus at the buried piezoresistor. The concentrations were well consistent with the theory. Near the surface, at less

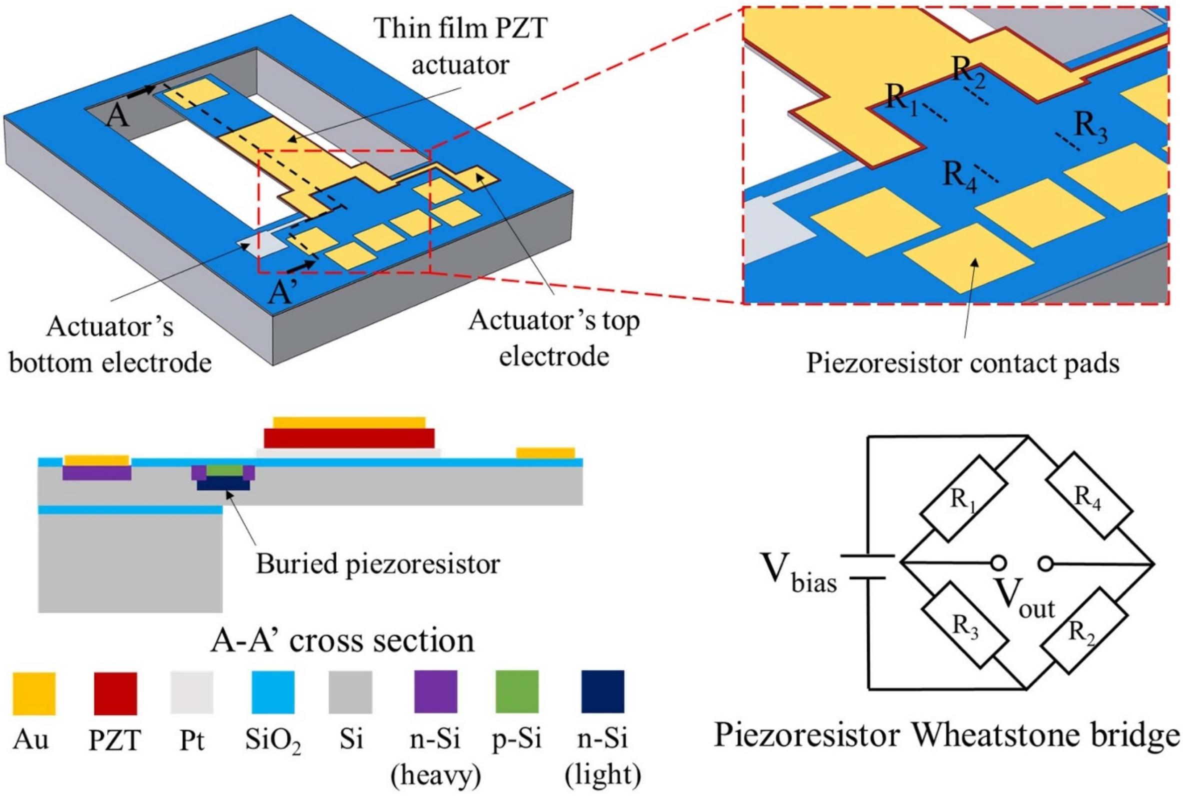

Figure 2. Device schematic. A 3D figure and cross section view of the device are shown on the left side. A close-up of the sensors area and electrical connection diagram are shown on the right side.

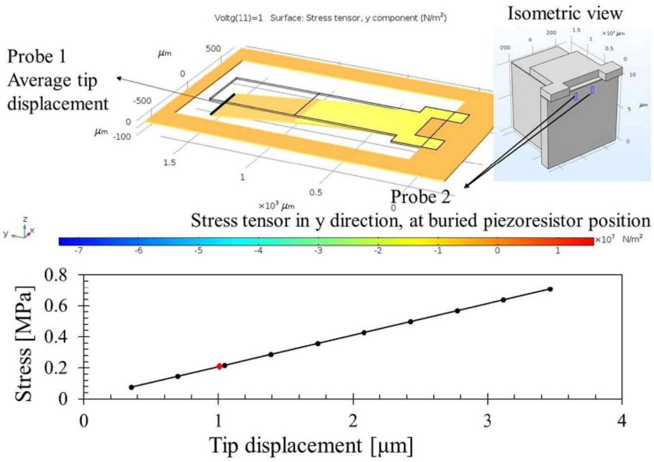

Figure 3. Static analysis by FEA. Model indicating probes position (top) and average stress in y direction at buried piezoresistor position (bottom).

than 200 nm depth, phosphorus is a major dopant. On the other hand, boron is distributed to the deeper area. Thus the p-type region was successfully buried in the Si layer.

The dynamic response of the device was measured by both laser Doppler velocimeter (LDV, MSA-500, Polytec GmBH, Germany) and the integrated piezoresistors. The actuation voltage to the PZT film was 1 V_{p-p} for both cases. Figure 7(a) shows the resistance of the piezoresistors for several chips, measured by multitester at rest condition. All piezoresistors should have been equal but significant mismatch in resistance was observed, likely due to fabrication error during the ion implantation stages. To compensate for this difference, the experimental setup shown in figure 7(b) was used. Piezoresistors R_3 and R_4 were replaced by external variable resistors $\widetilde{R}_3$ and $\widetilde{R}_4$ matching the values of R_1 and R_2, respectively. An actuation signal was generated from a lock-in amplifier (UHFLI, Zurich Instruments, Switzerland). The output signal from the bridge circuit was measured by the lock-in amplifier. The bias voltage to the bridge circuit, V_{bias}, was 10 V.

Figure 8(a) shows the LDV measurement result. The amplitude and phase of the oscillation at a point about 300 μm away from the fixed end was recorded. Figure 8(b) shows the output signal from the fabricated piezoresistors. The same resonance peak at 6.306 kHz was successfully observed and is consistent with the FEM simulation result of 6.768 kHz, proving that our buried piezoresistor could correctly detect the motion of the MEMS structure. Q-factors calculated from these measurements are $Q_{\text{LDV}} = 175.47$ and $Q_{\text{output}} = 173.99$.

Figure 9 shows the relationship between cantilever displacement and sensor output. The PZT actuator was driven at a constant frequency of 9 kHz, i.e. non-resonance. The voltage applied to the PZT actuator ranged from 1 V_{p-p} to 10 V_{p-p}. The displacement was measured by LDV. The expected values from the simple analytical model and FEA simulation are

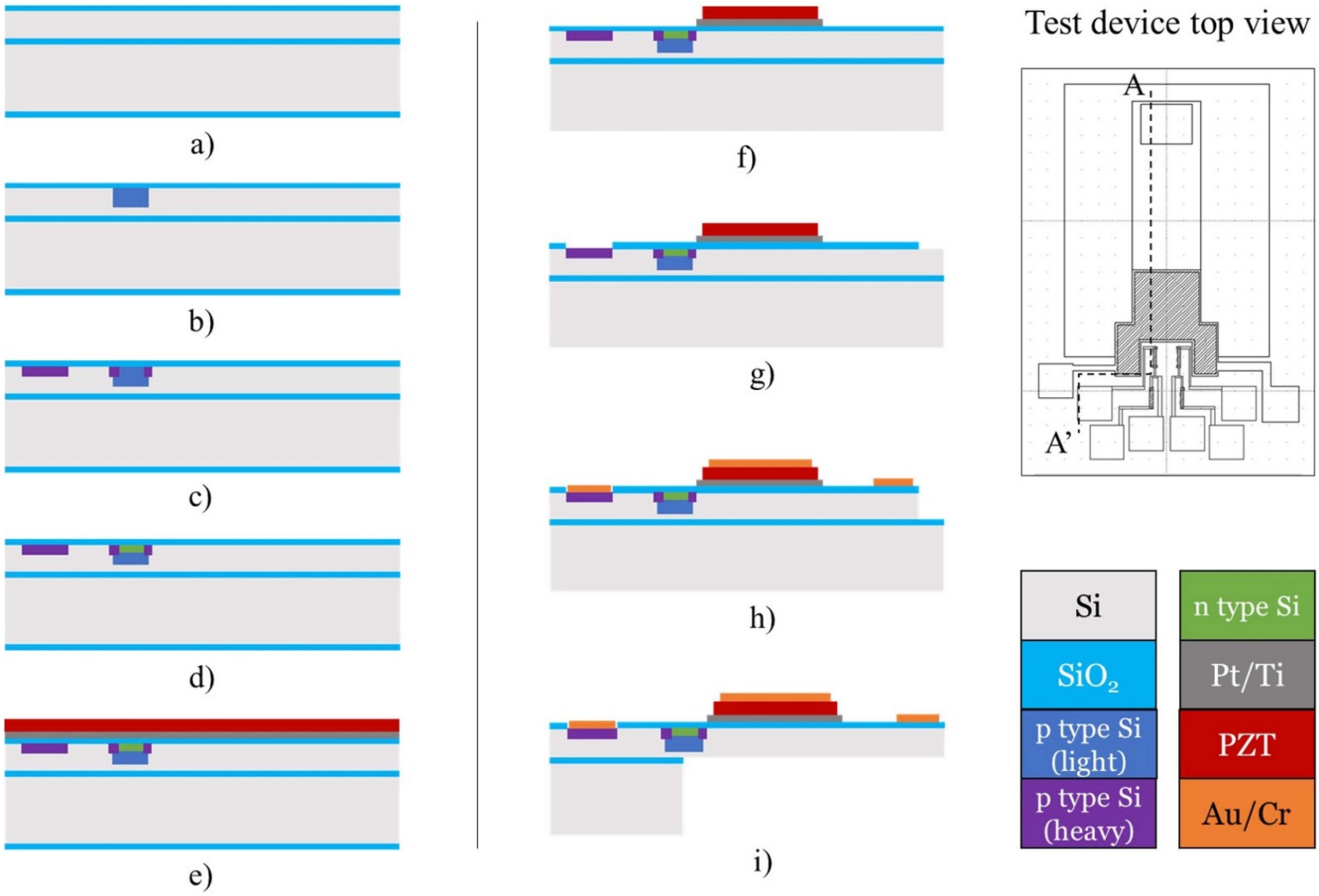

Figure 4. Fabrication process. First, buried piezoresistor implantation by (a) thermal oxidation of SOI wafer, (b) B light doping and drive-in annealing, (c) B heavy doping for electrical connection, (d) P implantation and rapid thermal annealing (RTA). Then actuator and structure formation by (e) deposition of Pt/Ti bottom electrode and PZT thin film, (f) etching of PZT (wet) and Pt/Ti (ion beam milling), (g) wet etching of SiO_2, (h) Au/Cr deposition by evaporation (top electrode and contact pads), patterned by lift-off and device layer Si etching by DRIE. Finally, structure release by (i) handle layer and buried oxide etching by DRIE and CCP-RIE.

also shown. As can be clearly seen, the sensor output was well proportional to the displacement of the cantilever. The sensitivity was about 0.037 mV μm^{-1}, which is 2.3% higher than the estimation derived from FEA results.

Figure 10 shows the electrical noise in the output signal. The signal output from the bridge circuit was amplified by an instrumentation amplifier using precision amplifiers OPA2604AP (Texas Instruments, USA). Noise floor was about 1×10^{-6} V/$\sqrt{\text{Hz}}$ under the bias voltage of $V_{\text{bias}} = 1$ V. No actuation signal was applied to the PZT. The red dotted line shows the output noise of the circuit obtained by SPICE-based circuit simulator (TINA TI, Texas Instruments).

5. Discussion

If precise position sensors can be monolithically integrated in a high-performance piezoelectric actuator, the long-term instability of the material can be compensated by the feedback control. With this idea in mind, the device presented in this work was designed along with the fabrication process to evaluate how both technologies (piezoresistive sensors and sol-gel PZT thin film) interact with each other (or not) during fabrication and operation. The test device design was kept as simple as possible to facilitate performance evaluation. The integrated piezoresistive sensors can certainly be optimized to improve sensitivity without requiring huge amplification or input voltage, but the obtained data satisfies the objective of proving compatibility between the sensors and actuator.

While we have not studied the effects that PZT integration could have on the well-known long-term stability of silicon piezoresistors, we think it unlikely. Unwanted diffusion from the PZT actuator is the major threat to the long-term stability of the sensors. Diffusion barriers combining SiO_2 and SiN_x are commonly used to protect piezoresistors from surface impurities and humidity, but the buried piezoresistor has its p-n junction too deep to be affected by natural diffusion at low temperatures.

The fabrication process presented here was developed to monolithically integrate buried piezoresistor and sol-gel PZT processes together, that had already been optimized independently in previous studies. For the PZT sol-gel deposition, thermally grown SiO_2 is preferred, rather than SiO_2

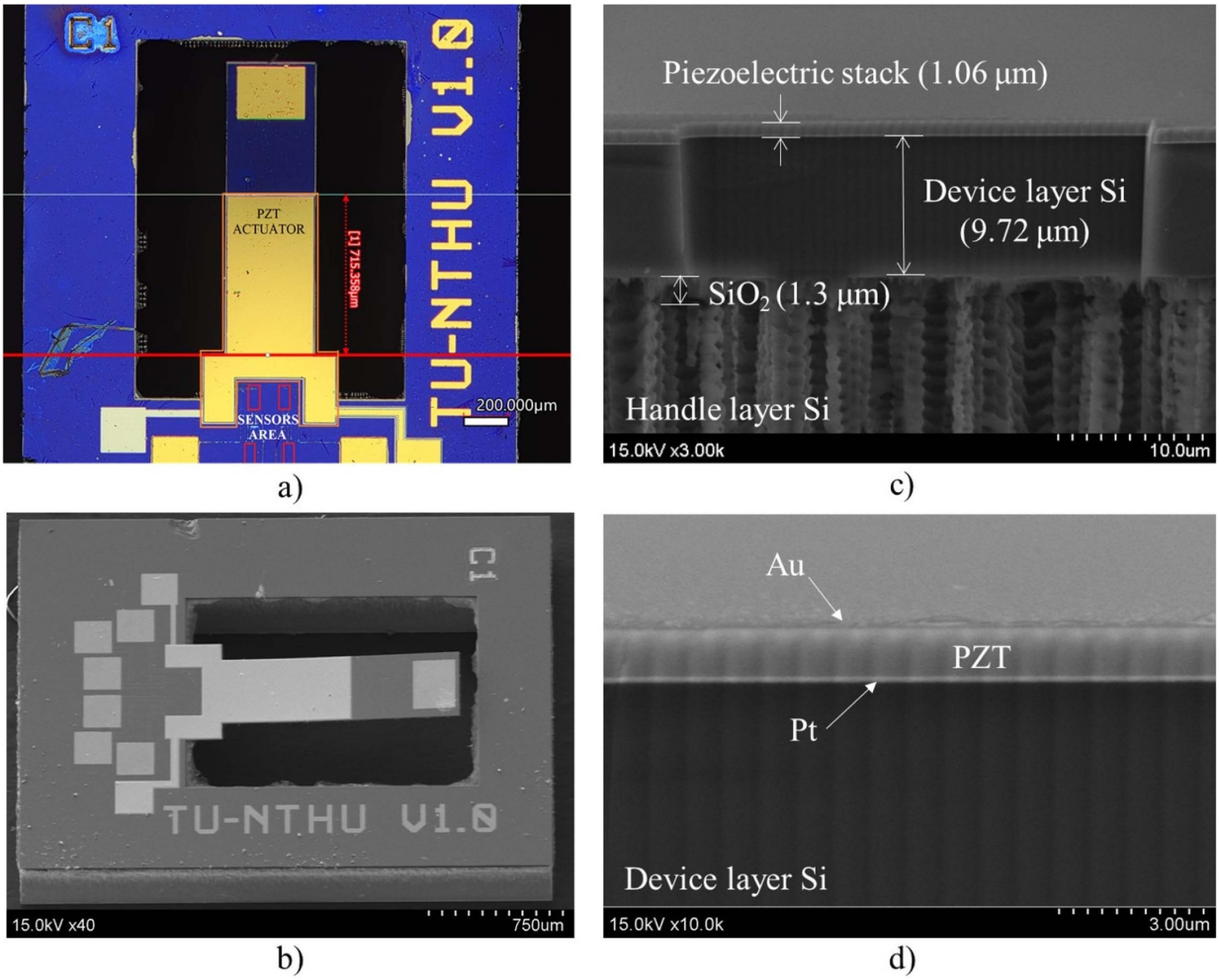

Figure 5. Finished cantilever test device. (a) Picture by optical microscope. (b) SEM picture. (c) Cross section on actuator area. (d) Close-up of piezoelectric stack cross section.

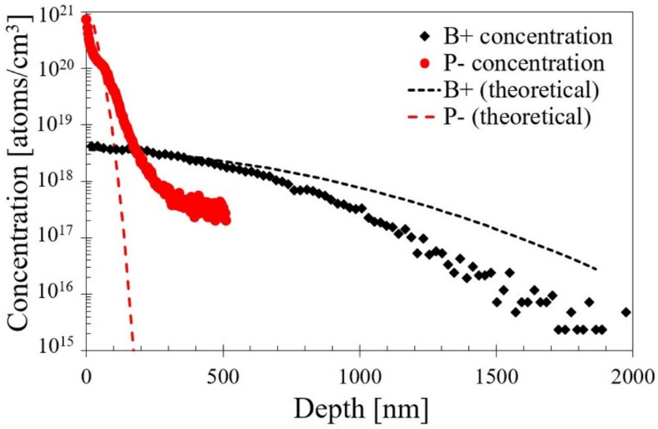

Figure 6. Dopant concentration profile on buried piezoresistor by SIMS analysis.

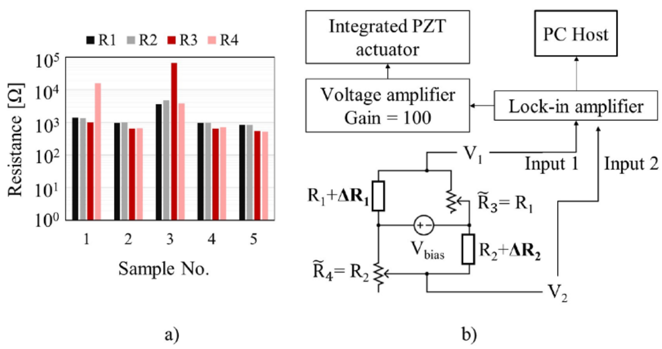

Figure 7. Buried piezoresistor evaluation. (a) Measured resistance of the four on-chip piezoresistors by multitester for 5 different chips. (b) Experimental setup for sensor evaluation, showing the modified Wheatstone bridge to overcome the resistance mismatch between the on-chip piezoresistors.

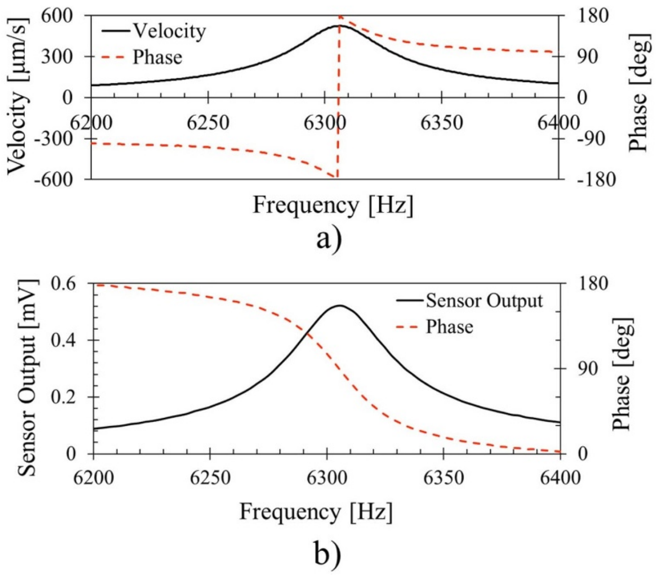

Figure 8. Dynamic evaluation of the device using (a) LDV and (b) fabricated buried piezoresistor.

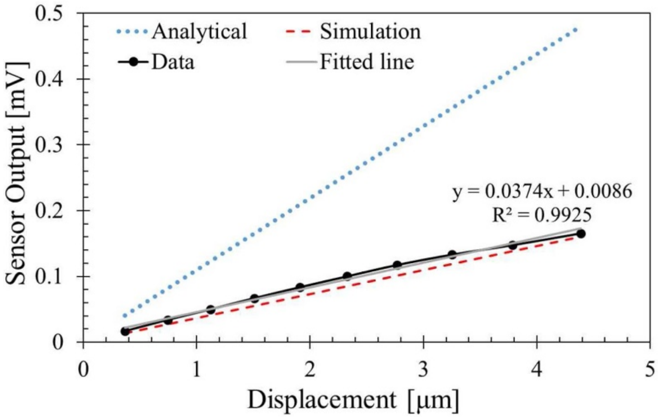

Figure 9. Sensitivity evaluation. Non-resonant actuation (9 kHz) at increasing unipolar voltage from 1 V to 10 V.

and SiN_x grown by CVD. However, the piezoresistors cannot stand for the high temperature during the thermal oxidation. Therefore, the thermal oxidation must be done prior to making the piezoresistors. A thinner film is convenient to make efficient ion implantation (less energy and dosage required to get the same concentration [37]), but thicker film is better for passivation. In this paper, 40 nm was selected for the thickness of SiO_2 to satisfy both requirements. From the experimental results, both piezoresistive sensor and PZT actuator could work as designed, which means the designed thickness of the SiO_2 was effective for both elements.

Dynamic evaluation shows clear relationship between actuation voltage and displacement measured both by LDV and integrated piezoresistors. The displacement was well proportional to the actuation voltage. The non-linearity was about 0.75%.

Measured sensitivity was about 34.1% than predicted by analytical calculation, which was too simplified, and about

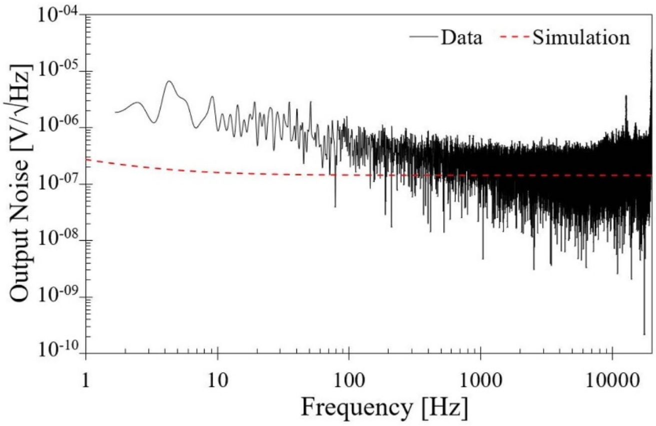

Figure 10. Electrical noise of output signal.

2.3% higher than the estimation derived from the FEA simulation. This is because the concentration of the impurity is not uniform as shown in figure 6, which means the piezoelectric coefficients have depth dependency. In addition, the stress applied to the piezoresistors also have depth dependency, with maximum value at the surface. For the estimations, average values were considered both for the impurity concentration and applied stress. When the output noise is assumed to be 4.5×10^{-9} V/$\sqrt{\text{Hz}}$, which is the theoretical noise density from the resistor, noise equivalent displacement (NED) becomes 0.12 nm/$\sqrt{\text{Hz}}$, which is enough for the precise displacement detection. Through the experimental noise analysis (figure 10), the output noise including the noise from amplifiers was about 1×10^{-6} V/$\sqrt{\text{Hz}}$ and NED becomes 27 nm/$\sqrt{\text{Hz}}$.

6. Conclusion

We have developed a PZT thin film actuator monolithically integrated with buried piezoresistors successfully. This is the first time such a combination is reported in detail. A fabrication process was proposed, and the compatibility was confirmed by experiments. The fabricated device could be driven by the thin film PZT actuator and the displacement could be detected by the buried piezoresistors. These results can be used for high-stability piezoelectric MEMS actuators with feed-back control of position, especially for applications where is necessary to keep a static position. The non-linearity of the sensor was 0.75% and the noise density was 27 nm/$\sqrt{\text{Hz}}$.

Acknowledgments

This study was supported by JSPS Grant-in-Aid for Scientific Research (B) No. 18H01390. Andrea Vergara was supported by Tohoku University GP-Mech Program.

ORCID iDs

Andrea Vergara https://orcid.org/0000-0002-8747-7092

Takashiro Tsukamoto https://orcid.org/0000-0002-7614-7717
Weileun Fang https://orcid.org/0000-0002-6000-026X

References

[1] Muralt P 2000 Ferroelectric thin films for micro-sensors and actuators: a review *J. Micromech. Microeng.* **10** 136–46
[2] Uchino K 2019 Introduction to piezoelectric actuators: research misconceptions and rectifications *Japan. J. Appl. Phys.* **58** SG0803
[3] Dubois M A and Muralt P 1998 PZT thin film actuated elastic fin micromotor *IEEE Trans. Ultrason. Ferroelectr. Freq. Control* **45** 1169–77
[4] Luginbuhl P, Collins S D, Racine G A, Gretillat M A, De Rooij N F, Brooks K G and Setter N 1997 Microfabricated Lamb wave device based on PZT sol-gel thin film for mechanical transport of solid particles and liquids *J. Microelectromech. Syst.* **6** 337–46
[5] Park J H, Lee H C, Park Y H, Kim Y D, Ji C H, Bu J U and Nam H J 2006 A fully wafer-level packaged RF MEMS switch with low actuation voltage using a piezoelectric actuator *J. Micromech. Microeng.* **16** 2281–6
[6] Mahameed R, Sinha N, Pisani M B and Piazza G 2008 Dual-beam actuation of piezoelectric AlN RF MEMS switches monolithically integrated with AlN contour-mode resonators *J. Micromech. Microeng.* **18** 105011
[7] Lee H C, Park J H, Park J Y, Nam H J and Bu J U 2005 Design, fabrication and RF performances of two different types of piezoelectrically actuated Ohmic MEMS switches *J. Micromech. Microeng.* **15** 2098–104
[8] Gross S J, Tadigadapa S and Jackson T N 2003 Lead-zirconate-titanate-based piezoelectric micromachined switch *Appl. Phys. Lett.* **83** 174–6
[9] Lee S S and White R M 1998 Piezoelectric cantilever acoustic transducer *J. Micromech. Microeng.* **8** 230–8
[10] Ko S C, Kim Y C, Lee S S, Choi S H and Kim S R 2003 Micromachined piezoelectric membrane acoustic device *Sensors Actuators* A **103** 130–4
[11] Chen S J, Choe Y, Baumgartel L, Lin A and Kim E S 2012 Edge-released, piezoelectric MEMS acoustic transducers in array configuration *J. Micromech. Microeng.* **22** 025005
[12] Stoppel F, Männchen A, Niekiel F, Beer D, Giese T and Wagner B 2018 New integrated full-range MEMS speaker for in-ear applications *2018 IEEE Micro Electro Mechanical Systems (MEMS)* pp 1068–71
[13] Cheng H H, Lo H H, Huang Z R, Wang Y J, Wu M and Fang W 2020 On the design of piezoelectric MEMS microspeaker for the sound pressure level enhancement *Sensors Actuators* A **306** 111960
[14] Clerici A R and Bottoni F 2018 MEMS loudspeaker having an actuator structure and a diaphragm spaced apart therefrom US Patent No. 9,980,051
[15] Clerici A R and Bottoni F 2018 MEMS loudspeaker with position sensor US Patent No. 10,045,136
[16] Clerici A R and Bottoni F 2018 MEMS loudspeaker arrangement comprising a sound generator and a sound amplifier US Patent No. 10,097,928
[17] Nicolas S, Allain M, Bridoux C, Fanget S, Lesecq S, Zarudniev M, Bolis S, Pouydebasque A and Jacquet F 2015 Fabrication and characterization of a new varifocal liquid lens with embedded PZT actuators for high optical performances *28th IEEE Int. Conf. on Micro Electro Mechanical Systems (MEMS)* pp 65–8
[18] Chen S H, Michael A and Kwok C Y 2018 A fast response MEMS piezoelectric microlens actuator with large stroke and low driving voltage *Proc. of the 13th Annual IEEE Int. Conf. on Nano/Micro Engineered and Molecular Systems* Singapore pp 199–203
[19] Tani M, Akamatsu M, Yasuda Y and Toshiyoshi H 2007 A two-axis piezoelectric tilting micromirror with a newly developed PZT-meandering actuator *IEEE 20th Int. Conf. on Micro Electro Mechanical Systems (MEMS)* Kobe, Japan pp 699–702
[20] Koh K H, Kobayashi T, Hsiao F L and Lee C 2010 Characterization of piezoelectric PZT beam actuators for driving 2D scanning micromirrors *Sensors Actuators* A **162** 336–47
[21] Naono T, Fujii T, Esashi M and Tanaka S 2015 Non-resonant 2-D piezoelectric MEMS optical scanner actuated by Nb doped PZT thin film *Sensors Actuators* A **233** 147–57
[22] Kanno I 2018 Piezoelectric MEMS: Ferroelectric thin films for MEMS applications *Japan. J. Appl. Phys.* **57** 040101
[23] Akamatsu M, Tani M and Yasuda Y 2002 Fast deposition of lead-zirconate-titanate thick films by arc discharged reactive ion-plating method *Japan. J. Appl. Phys.* **41** 6976–9
[24] Hishinuma Y, Fujii T, Naono T, Arakawa T and Li Y 2015 Recent progress on development of sputtered PZT film at FUJIFILM *Joint IEEE Int. Symp. on the Applications of Ferroelectric (ISAF), Int. Symp. on Integrated Functionalities (ISIF) and Piezoelectric Force Microscopy Workshop (PFM)* pp 288–91
[25] Holström S T S, Baran U and Urey H 2014 MEMS laser scanners: a review *J. Microelectromech. Syst.* **23** 259–75
[26] Lou X J and Wang J 2010 Bipolar and unipolar electrical fatigue in ferroelectric lead zirconate titanate thin films: An experimental comparison study *J. Appl. Phys.* **108** 034104
[27] Mazzalai A, Balma D, Chidambaram N, Matloub R and Muralt P 2015 Characterization and fatigue of the converse piezoelectric effect in PZT films for MEMS applications *J. Microelectromech. Syst.* **24** 831–8
[28] Bell D J, Lu T J, Fleck N A and Spearing S M 2005 MEMS actuators and sensors: observations on their performance and selection for purpose *J. Micromech. Microeng.* **15** S153–64
[29] Sasaki M, Tabata M, Haga T and Hane K 2006 Piezoresistive rotation angle sensor integrated in micromirror *Japan. J. Appl. Phys.* **45** 3789–93
[30] Yalcinkaya A D, Urey H, Brown D, Montague T and Sprague R 2006 Two-axis electromagnetic microscanner for high resolution displays *J. Microelectromech. Syst.* **15** 786–94
[31] Esashi M, Komatsu H and Matsuo T 1983 Biomedical pressure sensor using buried piezoresistor *Sensors Actuators* **4** 537–44
[32] Tsukamoto T, Asao H and Tanaka S 2017 Stylus type MEMS texture sensor covered with corrugated diaphragm *J. Micromech. Microeng.* **27** 095006
[33] Barlian A A, Park W T, Mallon J R, Rastega Jr A and Pruitt B L 2009 Review: Semiconductor piezoresistance for microsystems *Proc. IEEE* **97** 513–22
[34] Kanda Y 1982 A graphical representation of the piezoresistance coefficients in silicon *IEEE Trans. Electron Devices* **ED-29** 64–70
[35] Harley J A and Kenny T W 2000 1/F Noise considerations for the design and process optimization of piezoresistive cantilevers *J. Microelectromech. Syst.* **9** 226–35
[36] Moriyama M, Totsu K and Tanaka S 2019 Sol–gel deposition and characterization of lead zirconate titanate thin film using different commercial sols *Sensors Mater.* **31** 2497–509
[37] Gibbons J F 1968 Ion implantation in semiconductors - Part I Range distribution theory and experiments *Proc. IEEE* **56** 295–319